*Int. J. Heat Mass Transfer.* Vol. 25, No. 2, pp. 231–241, 1982
Printed in Great Britain

0017-9310/82/020231-11 $03.00/0
Pergamon Press Ltd.

# A NUMERICAL SOLUTION OF LAMINAR DEVELOPING FLOW IN ECCENTRIC ANNULAR DUCTS*

E. E. FELDMAN
Argonne National Laboratory, Argonne, IL 60439, U.S.A.

and

R. W. HORNBECK† and J. F. OSTERLE
Carnegie-Mellon University, Pittsburgh, PA 15213, U.S.A.

(*Received* 10 *September* 1980 *and in revised form* 21 *July* 1981)

**Abstract**—Laminar incompressible flow in straight ducts of eccentric annular cross section is analyzed. Numerical methods are used to solve an approximate hydrodynamic model, which was developed from the bipolar coordinate representation of the Navier–Stokes equations. Solutions obtained for the proposed model compare favorably with those of two alternative models and with published solutions for the concentric annulus and the circular tube. Results are presented for five different geometries.

## NOMENCLATURE

$a$, location of the positive pole of the bipolar coordinate system [m];
$D_h$, hydraulic diameter $2(r_{ow}-r_{iw})$[m];
$e$, absolute eccentricity, or center-to-center distance [m];
$h$, coordinate scale factor, defined by equation (11) [m];
$H$, dimensionless $h$, $h/D_h$,
$p$, thermodynamic pressure [Pa];
$P$, dimensionless $p$, $(p-p_e)/(\rho\bar{w}^2)$;
$PD$, pressure defect, defined by equation (37);
$r$, radius [m];
$r^*$, radius of the circle formed by the curve $\zeta=\zeta^*$ [m];
$Re$, Reynolds number, $\rho\bar{w}D_h/\mu$;
$t$, time [s];
$u$, $\zeta$ component of velocity [m/s];
$U$, dimensionless $u$, $\rho uD_h/\mu$;
$v$, $\eta$ component of velocity [m/s];
$V$, dimensionless $v$, $\rho vD_h/\mu$;
$\mathbf{V}$, velocity vector [m/s];
$w$, axial component of velocity [m/s];
$\bar{w}$, average $w$ (volume rate of flow per unit area) [m/s];
$W$, dimensionless $w$, $w/\bar{w}$;
$x, y$, Cartesian coordinates in the transverse plane [m];
$z$, axial coordinate [m];
$Z$, dimensionless $z$, $(z-z_e)/(D_hRe)$.

Greek symbols

$\gamma$, radius ratio, $r_{iw}/r_{ow}$;
$\Delta Z$, dimensionless axial step size;
$\varepsilon$, relative eccentricity, $e/(r_{ow}-r_{iw})$;
$\zeta, \eta$, bipolar coordinates in the annular cross-section;
$\zeta^*$, cylindrical surface of constant $\zeta$ along which the two transverse flows travelling away from the two walls are assumed to meet;
$\mu$, coefficient of viscosity [Pa.s];
$\rho$, density [kg/m$^3$].

Subscripts

e, entrance (inlet to the duct);
$i, j$, indices which together denote points of the finite difference grid ($i$ corresponds to $\zeta$ and $j$ to $\eta$);
iw, inner wall;
ow, outer wall;
max, maximum.

*Research performed at Carnegie-Mellon University, Pittsburgh, Pennsylvania.
†Deceased.

## 1. INTRODUCTION

THE FLOW entering a duct from a reservoir undergoes a development whereby the relatively flat inlet velocity profile gradually transforms into a fully developed profile. Flow developments which occur in the entrance region of ducts have been widely studied because they increase the duct pressure loss and alter the rate of heat transfer between the fluid and the duct wall. Lundgren *et al.* [1] devised a means of determining the pressure loss due to the entrance region in ducts of arbitrary cross-section. Sparrow and Lin [2], Murakawa [3], Heaton *et al.* [4], and Shumway and McEligot [5] analyzed the hydrodynamic entrance region of concentric annuli. The axial momentum equation for fully developed flow in eccentric annuli was solved by Redberger and Charles [6] with a numerical technique, and by Snyder and Goldstein [7] with a separation of variables technique. Hence, developing flow in concentric annuli and fully de-

veloped flow in eccentric annuli have been extensively studied. The only known solutions of the hydrodynamic entrance region problem for eccentric annuli are the finite difference solution of Feldman [8], which is the basis of this paper, and Wilson [9]. In the latter a linearized version of the governing equations is solved and the analysis leads to a 2-dim. eigenvalue problem. Although Galerkin's method is applied to this eigenvalue problem and shown to converge, the mathematical expressions containing the solution are not evaluated.

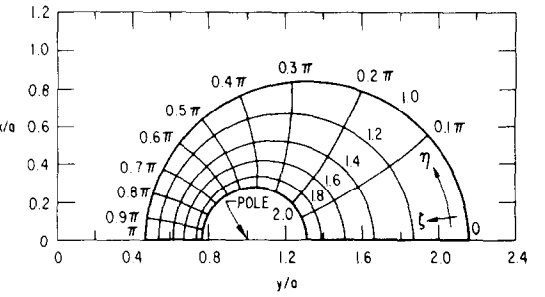


FIG. 1. Bipolar coordinate curves for the region $(1.0 \leq \zeta \leq 2.0, 0 \leq \eta \leq \pi)$.

## 2. MATHEMATICAL MODEL

The fluid is assumed to be incompressible, laminar and Newtonian, and to have constant properties. Body forces are neglected and only forced convection is considered. The vector form of the governing equations is:

continuity equation

$$\nabla \cdot \mathbf{V} = 0, \tag{1}$$

momentum equation

$$\rho \frac{D\mathbf{V}}{Dt} = -\nabla p + \mu \nabla^2 \mathbf{V}, \tag{2}$$

where $\mathbf{V}$ is velocity, $t$ is time, $\rho$ is density, $p$ is thermodynamic pressure, and $\mu$ is the coefficient of viscosity.

In the analysis of flow in eccentric annuli, it is convenient to represent the governing equations in the bipolar coordinate system. The bipolar coordinates $(\zeta, \eta)$ are related to the Cartesian coordinates $(x, y)$ by the following two equations:

$$\left(\frac{x}{a}\right)^2 + \left(\frac{y}{a} - \coth \zeta\right)^2 = \operatorname{csch}^2 \zeta \quad \text{for } -\infty < \zeta < \infty, \tag{3}$$

$$\left(\frac{x}{a} - \cot \eta\right)^2 + \left(\frac{y}{a}\right)^2 = \csc^2 \eta \quad \text{for } 0 \leq \eta \leq 2\pi. \tag{4}$$

Figure 1 shows curves of constant $\zeta$ and constant $\eta$ plotted as functions of $x$ and $y$. In the figure the positive pole is shown to be located on the $y/a$ axis at $y = a$. The constant $\zeta$ curves form a family of eccentric circles which are orthogonal to the family of constant $\eta$ curves. The constant $\zeta$ curves encircle the pole and the constant $\eta$ curves are circles which intersect it.

The geometry of any eccentric annulus can be characterized by the dimensionless pair of radius ratio, $\gamma$, and relative eccentricity, $\varepsilon$, which are given by:

$$\gamma = \frac{r_{iw}}{r_{ow}}, \tag{5}$$

$$\varepsilon = \frac{e}{r_{ow} - r_{iw}}, \tag{6}$$

where the subscripts iw and ow correspond to the inner and outer wall of the annulus, respectively, $r$ is the wall radius, and $e$ is the absolute eccentricity, or center-to-center distance, of the annulus. From equation (3), one observes that each constant $\zeta$ curve is of radius csch $\zeta$ and has its center located on the $x/a$ axis at $y/a = \coth \zeta$. Therefore, $r_{iw}$, $r_{ow}$, and $e$ of equations (5) and (6) can be replaced by $a \cdot (\operatorname{csch} \zeta_{iw})$, $a \cdot (\operatorname{csch} \zeta_{ow})$, and $a \cdot (\coth \zeta_{ow} - \coth \zeta_{iw})$, respectively. With the aid of a few hyperbolic function identities, one can express equations (5) and (6) solely in terms of $\gamma$, $\varepsilon$, $\cosh \zeta_{ow}$ and $\cosh \zeta_{iw}$. When the resultant pair of simultaneous equations is solved, the following two expressions, which can also be found in [7], are obtained. Hence

$$\cosh \zeta_{ow} = \frac{\gamma(1 - \varepsilon^2) + (1 + \varepsilon^2)}{2\varepsilon}, \tag{7}$$

$$\cosh \zeta_{iw} = \frac{\gamma(1 + \varepsilon^2) + (1 - \varepsilon^2)}{2\varepsilon\gamma}. \tag{8}$$

Values of $\varepsilon$ and $\gamma$, which by definition are both between 0 and 1.0, can be used in the above two equations to find values of $\zeta_{ow}$ and $\zeta_{iw}$. Planar symmetry enables us to consider only the half of the annulus which is between $\eta = 0$ and $\eta = \pi$. Hence the region of interest is $(\zeta_{ow} \leq \zeta \leq \zeta_{iw}, 0 \leq \eta \leq \pi)$.

The general orthogonal curvilinear coordinate expressions for the vector operators of equations (1) and (2) along the necessary bipolar coordinate scale factors can be found in [10]. These enable the continuity equation and the three vector components of the momentum equation to be represented in the bipolar coordinate system. Unfortunately, no practical means appears to exist which would allow one to solve the resultant four simultaneous partial differential equations in their entirety. Therefore, these equations will be used in the development of an approximate model.

In the model development, knowledge of the relative magnitudes of the individual terms of the four scalar equations will enable one to judge the relative importance of each term. The values of the terms vary throughout the entrance region and cannot be known on a local basis unless the solution of the equations is known. One can, however, determine in a global sense relative magnitudes of the terms which represent averages taken over the entire entrance region. If we

assume that the global magnitude of a term is a measure of the impact it will have on the solution, then we can assess the degree of approximation involved in eliminating that term. This order of magnitude analysis can be found in [8] where it is assumed that the ratio of the length of the entrance region to the duct hydraulic diameter is much greater than 1. For this ratio to be at least 10, for example, the entrance length values presented in Table 1 of Section 5 indicate that the minimum Reynolds number would typically be between 30 and 1000, depending upon annular geometry. Since, as indicated below, the model ignores transverse pressure gradients and assumes a uniform inlet velocity profile, the minimum acceptable Reynolds number is expected to be a few hundred rather than 30 and the solution is not expected to be accurate extremely close to the duct inlet. The order of magnitude analysis leaves the continuity equation unaltered and causes a reduced form of the axial momentum equation to replace all three scalar components. The continuity equation and the reduced momentum equation, expressed in bipolar coordinates, are:

$$\frac{\partial}{\partial\zeta}(hu) + \frac{\partial}{\partial\eta}(hv) + \frac{\partial}{\partial z}(h^2 w) = 0, \tag{9}$$

$$\rho\left[\frac{u}{h}\frac{\partial w}{\partial\zeta} + \frac{v}{h}\frac{\partial w}{\partial\eta} + w\frac{\partial w}{\partial z}\right] = -\frac{\mathrm{d}p}{\mathrm{d}z} + \frac{\mu}{h^2}\left[\frac{\partial^2 w}{\partial\zeta^2} + \frac{\partial^2 w}{\partial\eta^2}\right], \tag{10}$$

where

$$h = \frac{a}{\cosh\zeta - \cos\eta}, \tag{11}$$

$z$ is the axial coordinate, $u$, $v$ and $w$ are the $\zeta$, $\eta$ and $z$ components of velocity, and $a$ is the location of the pole (refer to Fig. 1). The boundary conditions for equations (9) and (10) are that all three components of velocity, $u$, $v$ and $w$, are zero at $\zeta = \zeta_{ow}$ and at $\zeta = \zeta_{iw}$.

While $u$, $v$ and $w$ in equations (9) and (10) are functions of $\zeta$, $\eta$ and $z$, the pressure gradient $\mathrm{d}p/\mathrm{d}z$ is a total derivative which is a function of only $z$. Since there are three unknown components of velocity in addition to the pressure gradient, equations (9) and (10) do not form a complete mathematical model. Carlson and Hornbeck [11] faced a similar situation in the solution of the hydrodynamic entrance region of a duct of square cross-section. They developed a relationship between the two transverse velocity components in the square cross-section by assuming that all of the transverse flow was directed along straight lines which cross the center of the duct. Brief consideration of the mechanism which produces the transverse flow in an annular duct will provide substantial information about its path. When a flow with a uniform axial profile and no transverse components enters a circular tube, the flow near the wall is retarded and transverse flow is sent radially and symmetrically toward the center. Similarly, external axial flow along the lateral surface of a cylinder produces radial symmetric transverse flow away from the center of the cylinder. If the cylinder is placed inside the tube to form a concentric annulus, the two transverse flows will meet and go to zero along a surface of revolution. If we think in terms of two boundary layers simultaneously forming along the two walls, then this surface must fall between the two boundary layers and a reasonable approximation to it is the cylindrical surface of constant radius which intersects the ridge of maximum axial velocities for fully developed flow. At axial locations far from the duct inlet this representation is exact and near the duct inlet it is reasonable.

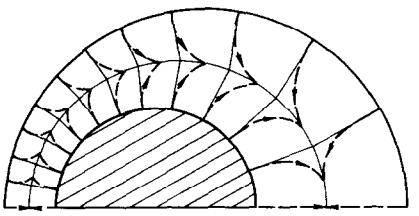

FIG. 2. Transverse flow description.

In the eccentric case, a similar mechanism prevails. Figure 2 depicts the expected paths of the transverse flow. If the transverse flow of either surface could behave independently of the other surface, it would follow the radial lines emanating from its surface. The presence of the other surface, however, causes the transverse flows of each surface to bend away from their respective radial lines. As the two flows approach each other, they travel along paths which tend to transfer flow from the narrower side of the annulus to the wider side. The surface along which the two transverse flows merge, by similar arguments to those proposed for the concentric case, can be approximated by the cylindrical surface which intersects the ridge of maximum axial velocity for fully developed flow. For the sake of mathematical simplicity, this surface is approximated by one of constant radius, $r^*$. In reality, as the absolute eccentricity increases, the curve in question deviates significantly from one of constant radius and tends to become egg-shaped. Fortunately, as demonstrated in Section 4, the solution is only very mildly sensitive to the choice of transverse flow prescription.

For a concentric annulus the classical closed-form representation of $r^*$ is $r_{ow}\sqrt{(1-\gamma^2)/\ln(1/\gamma^2)}$. This representation is also used to approximate $r^*$ for all but the most eccentric geometry ($\varepsilon = 0.9$, $\gamma = 0.1$) considered in the present analysis. The use of the above $r^*$ representation in this extreme case causes the circle formed by the $r^*$ curve not to include the center of the curve defining the outer wall. This causes the radial lines emanating from the inner and outer walls not to intersect in the manner depicted in Fig. 2 and hence the model breaks down. Therefore, in this case, $r^*$ is arbitrarily taken to be half of the radius of the outer wall.

Based on the above description and assumptions, a mathematical relationship for the transverse velocity ratio, $v/u$, was developed and is

For $\zeta \neq \zeta^*$

$$\frac{v}{u} = F\frac{t_2 - t_1}{1 + t_2 t_1}, \tag{12}$$

$$F = \begin{cases} \dfrac{\operatorname{csch}\zeta_{ow} - \operatorname{csch}\zeta^*}{\operatorname{csch}\zeta - \operatorname{csch}\zeta^*} & \text{for } \zeta < \zeta^*, \\ \dfrac{\operatorname{csch}\zeta_{iw} - \operatorname{csch}\zeta^*}{\operatorname{csch}\zeta - \operatorname{csch}\zeta^*} & \text{for } \zeta > \zeta^*, \end{cases} \tag{13}$$

$$t_2 = \frac{H\sinh\zeta}{\dfrac{0.5}{1-\gamma}(\sinh\zeta_{ow})(\cot\eta) - H\sin\eta}, \tag{14}$$

$$t_1 = \begin{cases} \dfrac{H\sin\eta}{H\sinh\zeta - \dfrac{0.5}{1-\gamma}\cosh\zeta_{ow}} & \text{for } \zeta < \zeta^*, \\ \dfrac{H\sin\eta}{H\sinh\zeta - \dfrac{0.5}{1-\gamma}\cosh\zeta_{iw}} & \text{for } \zeta > \zeta^*, \end{cases} \tag{15}$$

where $\zeta^*$ is the $\zeta$ curve of radius $r^*$ and $H$ is the dimensionless form of $h$ and given by

$$H = \frac{0.5\sinh\zeta_{ow}}{(1-\gamma)(\cosh\zeta - \cos\eta)}. \tag{16}$$

For $\zeta = \zeta^*$

$$u = 0. \tag{17}$$

Equations (9)–(17) together with the zero-velocity boundary conditions and a uniform inlet velocity profile provide a complete mathematical model of the hydrodynamic entrance region. As is well documented by Hornbeck [12], however, several hydrodynamic entrance region solutions including those for parallel plates [13], a circular tube [14], and a square duct [11], have also used the integral form of the continuity equation. The models in these solutions are similar to the current one in that they all contain the differential form of the continuity equation, a reduced axial momentum equation in which the pressure gradient is a total derivative, and, in the square duct case, a transverse flow model. Of course, since the integral form of the continuity equation can be obtained by applying the divergence theorem to the differential form, the integral form is mathematically redundant. In the finite difference solution, however, this redundancy is avoided because the differential form is not represented in all nodal regions close to the duct walls. The bipolar coordinate form of the integral continuity equation is

$$\frac{\pi}{2}a^2(1-\gamma^2)\bar{w}\operatorname{csch}^2\zeta_{ow} = \int_0^{\pi}\int_{\zeta_{iw}}^{\zeta_{ow}} wh^2 d\zeta\, d\eta, \tag{18}$$

where $\bar{w}$ is the average axial velocity taken as the volume rate of flow per unit of cross-sectional area. Equation (18) is particularly useful because it represents a physical constraint which does not include the transverse velocity components.

## 3. METHOD OF SOLUTION

The equations of the model are expressed in dimensionless form with $u$, $v$, $w$, $p$, $z$ and $h$, respectively represented by:

$$U = \frac{\rho u D_h}{\mu}, \tag{19}$$

$$V = \frac{\rho v D_h}{\mu}, \tag{20}$$

$$W = \frac{w}{\bar{w}}, \tag{21}$$

$$P = \frac{p - p_e}{\rho\bar{w}^2}, \tag{22}$$

$$Z = \frac{z - z_e}{D_h Re}, \tag{23}$$

$$H = \frac{h}{D_h}, \tag{24}$$

where the subscript e of $z_e$ and $p_e$ corresponds to the entrance of the duct, and $D_h$ and $Re$ are the hydraulic diameter and the Reynolds number, respectively, and are given by

$$D_h = 2(r_{ow} - r_{iw}) = 2a(1-\gamma)\operatorname{csch}\zeta_{ow}, \tag{25}$$

$$Re = \frac{\rho\bar{w}D_h}{\mu}. \tag{26}$$

With these definitions one may express the continuity equation, equation (9), and the axial momentum equation, equation (10), respectively, as

$$\frac{\partial}{\partial\zeta}(HU) + \frac{\partial}{\partial\eta}(HV) + \frac{\partial}{\partial Z}(H^2W) = 0, \tag{27}$$

$$\frac{U}{H}\frac{\partial W}{\partial\zeta} + \frac{V}{H}\frac{\partial W}{\partial\eta} + W\frac{\partial W}{\partial Z} = -\frac{dP}{dZ} + \frac{1}{H^2}\left[\frac{\partial^2 W}{\partial\zeta^2} + \frac{\partial^2 W}{\partial\eta^2}\right]. \tag{28}$$

In equation (12), $v/u$ equals $V/U$ and all other variables in equations (12)–(16) are already dimensionless. Thus equations (13)–(16) remain unchanged and equations (12) and (17) become

$$\frac{V}{U} = F\frac{t_2 - t_1}{1 + t_2 t_1} \quad \text{for } \zeta \neq \zeta^*, \tag{29}$$

$$U = 0 \quad \text{for } \zeta = \zeta^*. \tag{30}$$

The dimensionless form of the boundary conditions is that at $\zeta = \zeta_{ow}$ and at $\zeta = \zeta_{iw}$, $U = V = W = 0$. Equations (23) and (21) provide that at the duct inlet $Z = 0$ and $W = 1$ at all interior values of $\zeta$. The dimensionless representation of the integral form of the continuity equation, equation (18), is:

$$\frac{8}{\pi}\frac{1-\gamma}{1+\gamma}\int_0^{\pi}\int_{\zeta_{ow}}^{\zeta_{iw}} WH^2 \mathrm{d}\zeta\,\mathrm{d}\eta = 1. \tag{31}$$

A finite difference solution to the model is obtained from a numerical marching technique in which the hydrodynamic entrance region is sectioned into a series of parallel planes which are perpendicular to the $Z$ axis. At the inlet, the flow is taken to have a uniform axial profile and no transverse velocity components. The hydrodynamic model is solved at the first plane beyond the inlet independently of all succeeding planes. The solution for the second plane depends only upon that for the first and, similarly, the solution for the $k + 1$ plane depends only upon that for its immediate predecessor, the $k$ plane. Thus, the entire hydrodynamic entrance region is solved by solving one plane at a time in succession. In each plane, the region defined by ($\zeta_{ow} \le \zeta \le \zeta_{iw}$, $0 \le \eta \le \pi$) is sectioned by sets of constant $\zeta$ curves (with index $i$) and constant $\eta$ curves (with index $j$) to form a finite difference grid covering half of the symmetric annular cross section. This grid is chosen to be sufficiently fine to enable solutions with acceptably small truncation errors to be produced without requiring excessive amounts of computing time and storage. The $\zeta$ interval from $\zeta_{ow}$ to $\zeta^*$ and the one from $\zeta_{iw}$ to $\zeta^*$ are each divided into the 16 proportions which, starting from either wall, are 0.01, 0.01, 0.02, 0.02, 0.02, 0.02, 0.05, 0.05, 0.1, 0.1, 0.1, 0.1, 0.1, 0.1, 0.1, 0.1. Thus the $\zeta$ grid size adjacent to the outer wall is $0.01 \cdot (\zeta^* - \zeta_{ow})$ and the one adjacent to the inner wall is $0.01 \cdot (\zeta_{iw} - \zeta^*)$. The very small grid spacing at the walls accommodates the steep velocity gradients that occur there. The $\eta$ interval from 0 to $\pi$ is divided into 24 equal segments. Therefore, there are 775, i.e. $(2 \times 16 - 1) \cdot (24 + 1)$, interior grid points, with indices $(i, j)$, for which values of the three components of velocity, $U_{i,j}$, $V_{i,j}$ and $W_{i,j}$, are required and 25 points on each $\zeta$ boundary for which all values of $U_{i,j}$, $V_{i,j}$, and $W_{i,j}$ are zero.

In the finite difference representation of equation (28) at the $k + 1$ plane, all velocity coefficients of derivatives are evaluated in the $k$ plane, and only the derivatives with respect to $\zeta$ and $\eta$ are expressed in the $k + 1$ plane. A simple 1st-order backward difference, which uses values in both planes, is employed to approximate the axial derivatives. When equation (28) is represented at all 775 interior points of a plane, a simultaneous set of 775 equations containing 775 unknown values of $W_{i,j}$ and one unknown value of $\mathrm{d}P/\mathrm{d}Z$ are produced. There are an even number of equal $\eta$ intervals and all $\zeta$ intervals are in pairs of equal size. Therefore, Simpson's 1/3 rule can be used to approximate the double integral of equation (31). The finite difference representation of equation (31) completes the set of 776 simultaneous linear equation and unknowns.

A finite difference approximation provided by Allen [15] for grids of equal spacing and extended in [8] to grids of unequal spacing is used to approximate the $\zeta$ and $\eta$ derivatives of equation (28). The general form of this finite difference approximation is:

$$\left(\frac{\partial^2 S}{\partial \psi^2} + \lambda\frac{\partial S}{\partial \psi}\right)_l \approx \lambda\frac{-S_{l-1} + (1-\tau)S_l + \tau S_{l+1}}{(\psi_l - \psi_{l-1}) + \tau(\psi_{l+1} - \psi_l)}, \tag{32}$$

$$\tau = \frac{1 - \exp[\lambda(\psi_l - \psi_{l-1})]}{1 - \exp[-\lambda(\psi_{l+1} - \psi_l)]}, \tag{33}$$

where the dependent variable $S$ is a function of the independent variable $\psi$, $\lambda$ is a constant, and $l - 1$, $l$, and $l + 1$ are the indices of three consecutive points of increasing value in the $\psi$ finite difference grid. It can be shown, with the aid of L'Hôpital's rule for indeterminate forms, that if $\lambda = 0$, equation (32) is identical to the familiar central-difference representation of the second derivative which can be obtained from a 2nd-order Taylor series approximation.

If $\mathrm{d}P/\mathrm{d}Z$ were known, the 775 simultaneous linear equations produced at each plane by equation (28) could be solved by the method of successive over-relaxation (S.O.R.). Since at each plane $\mathrm{d}P/\mathrm{d}Z$ is unknown, appropriate guesses for all 776 unknowns are made and the following algorithm is used.

1. All 775 $W_{i,j}$'s are updated by performing an iteration by the method of S.O.R. on all 775 equations produced by equation (28).
2. All 776 unknowns are updated by dividing each by the numerical approximation of the left-hand side of equation (31).
3. The above two steps are repeated.
4. If

$$0 < \frac{\left(\frac{\mathrm{d}P}{\mathrm{d}Z}\right)_3 - \left(\frac{\mathrm{d}P}{\mathrm{d}Z}\right)_2}{\left(\frac{\mathrm{d}P}{\mathrm{d}Z}\right)_2 - \left(\frac{\mathrm{d}P}{\mathrm{d}Z}\right)_1} < 1, \tag{34}$$

where the subscripts 1, 2 and 3 refer to the latest three iterates in order of oldest to newest, then the current value of $\mathrm{d}P/\mathrm{d}Z$ is replaced by

$$\frac{\mathrm{d}P}{\mathrm{d}Z} = \left(\frac{\mathrm{d}P}{\mathrm{d}Z}\right)_3 - \frac{\left[\left(\frac{\mathrm{d}P}{\mathrm{d}Z}\right)_3 - \left(\frac{\mathrm{d}P}{\mathrm{d}Z}\right)_2\right]^2}{\left(\frac{\mathrm{d}P}{\mathrm{d}Z}\right)_3 - 2\left(\frac{\mathrm{d}P}{\mathrm{d}Z}\right)_2 + \left(\frac{\mathrm{d}P}{\mathrm{d}Z}\right)_1}. \tag{35}$$

5. The above four steps are repeated until the absolute value of the S.O.R. residual of largest magnitude in step 1 is smaller than a specified value.

Although a uniform profile of $W = 1$ identically satisfies equation (31), it only approximately satisfies the numerical representation of equation (31). Hence, at the duct inlet $W$ was increased slightly to avoid a numerically induced flow discontinuity between the

inlet and the first solution plane. This value of $W$ and an arbitrarily chosen negative value of $dP/dZ$ were used at the first solution plane to start the algorithm. At each succeeding plane, the algorithm was started with the solution of its immediate predecessor.

Step 4 increased the rate of convergence of the $dP/dZ$ iterates, which had been much slower than that of the $W_{i,j}$ iterates, by about an order of magnitude. Equation (35) of step 4 is Aitken's $\Delta^2$ formula [16] algebraically expressed in a form suggested by Westlake [17]. This form is well suited for evaluation by computers which set the quotient in equation (35) to zero when the divisor is zero, thereby leaving the latest $dP/dZ$ unchanged. Criterion (34) was included because equation (35) can produce an extremely bad iterate of $dP/dZ$ when the magnitude of the difference of successive iterates is not declining. An S.O.R. acceleration parameter in step 1 of 1.6 and a convergence criterion in step 5 of $10^{-6}$ were found to produce reasonably fast convergence to an accurate solution and were generally used.

After all $W_{i,j}$ for a plane are obtained, the numerical approximation to equation (27) is used in conjunction with equations (29) and (30) to directly evaluate without iteration all of the unknown $U_{i,j}$ and $V_{i,j}$ in the plane. First-order backward and forward differences are used almost exclusively in the numerical representation of equation (27).

At each plane $dP/dZ$ is used to approximate $P$ and the pressure defect, $PD$. The 1st-order backward-difference representation of $dP/dZ$ at the $k+1$ plane yields

$$P_{k+1} \approx P_k + \left(\frac{dP}{dZ}\right)_{k+1} (Z_{k+1} - Z_k), \qquad (36)$$

where the subscripts $k$ and $k+1$ refer to two successive planes. The pressure defect, or incremental pressure drop number, at any plane is approximated by

$$PD = -2\left[P - \left(\frac{dP}{dZ}\right)_{\infty} Z\right], \qquad (37)$$

where $(dP/dZ)_{\infty}$ is the fully developed flow value of $dP/dZ$. The asymptotic value which $PD$ approaches as the flow becomes fully developed will be referred to as the total pressure defect.

Near the duct inlet very small axial steps sizes, $\Delta Z$, of no larger than $0.25 \times 10^{-5}$ were used to accommodate the steep axial gradients which normally occur at the inlet. The inlet $\Delta Z$ was gradually increased with increasing $Z$ to a maximum $\Delta Z$ of 0.001. As a test of the adequacy of these prescribed step sizes, all of the step sizes used to solve the geometry ($\varepsilon = 0.5, \gamma = 0.5$) were multiplied by 0.05 and these reduced step sizes were used to re-evaluate the initial portion of the entrance region. The close agreement between these two solutions provides additional confidence in the ability of the larger step sizes to yield accurate results. Typically, 560–640 axial steps, requiring about 24–30 min of computing time on the Univac 1108 computer at the Carnegie-Mellon University Computation Center, were needed to obtain a complete hydrodynamic entrance region solution. A detailed listing of the FORTRAN IV computer programs and additional information concerning the solution method can be found in [8].

## 4. VERIFICATION OF THE MODEL

The principal assumption of the hydrodynamic model is that the axial velocity and pressure distributions are only moderately sensitive to the transverse flow distribution. If this assumption is valid, then other transverse flow distribution models should produce similar results. Therefore, two alternative models are identified and the results obtained with all three are compared.

In the first alternate model all of the transverse flow is assumed to be along curves of constant $\eta$. This is compatible with the general boundary layer development along the walls and has the advantage of being independent of the surface $\zeta = \zeta^*$, along which in the proposed model the transverse flows from the two walls meet. The mathematical representation of this alternate model contains the same continuity and momentum equations as the proposed model except that $V$ is set to zero. The disadvantage of this alternate model is that its lack of a velocity component in the $\eta$ direction is physically unrealistic. Since the axial velocity profile at the inlet is uniform, the $\eta$ component of velocity is needed to transfer flow from the narrowest to the widest part of the annular gap so that when the flow is fully developed the velocities along the ridge of maximum axial velocities increase monotonically from one side of the annular gap to the other.

While there are fundamental differences between the transverse flow descriptions of the proposed and first alternate models, there are also basic similarities. Both models satisfy the differential form of the continuity equation and have a transverse flow which perpendicularly meets both walls of the annulus. The second alternate model, however, is designed to be substantially different from either of the other two models. This difference enables the sensitivity of the hydrodynamic solutions to the choice of transverse flow description to be further assessed. In the second alternate there is no transverse flow and the mathematical representation of the model consists of equations (31) and (28) with $U$ and $V$ set to zero. Since this model does not satisfy the differential form of the continuity equation, it cannot be expected to produce results which are as accurate as those of the other two models.

Symmetry requires that all of the transverse flow in a concentric annulus be along symmetric radial lines. Because this is predicted by both the proposed model and the first alternate model and because we are seeking solutions for eccentric geometries, the highly eccentric geometry ($\varepsilon = 0.9, \gamma = 0.1$) was chosen for the comparison of the behaviors of the three models.

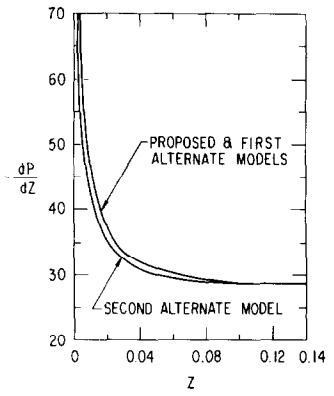


FIG. 3. Dimensionless axial pressure gradient ($\varepsilon = 0.9$, $\gamma = 0.1$).

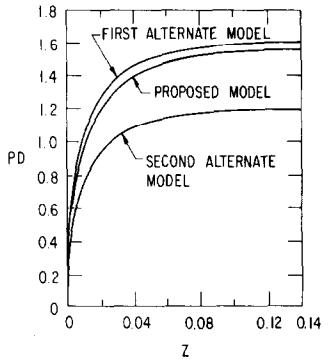


FIG. 4. Pressure defect ($\varepsilon = 0.9$, $\gamma = 0.1$).

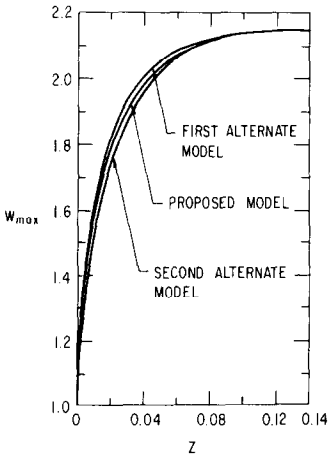


FIG. 5. Maximum dimensionless axial velocity ($\varepsilon = 0.9$, $\gamma = 0.1$).

This geometry enables a severe test of the models and strongly accentuates their differences.

Figures 3–5 compare axial distributions of $-dP/dZ$, $PD$, and maximum $W$ ($W_{max}$) for the three models. Generally, small differences in behavior are observed, particularly between the proposed and first alternate models. The total pressure defect for the proposed, first alternate and second alternate models, respectively, are 1.571, 1.622, and 1.205. If the entrance length is taken to be the value of $Z$ at which $W_{max}$ is 99% of its fully developed flow value, then the corresponding values of entrance length are $Z$ = 0.106, 0.104, and 0.099. The average, or apparent, Fanning friction factor between the duct inlet and the axial location $Z$ is given by $-P/(2ZRe)$. For $Z = 0.1$, which is about equal to the entrance length, the average friction factor of the first and second alternate models differ from that of proposed model by only 0.6% and −4.8%, respectively.

Published solutions for the two extremes of absolute eccentricity, i.e. $e = 0$ and $e = r_{ow}$, are another means of verification. The $e = 0$ extreme is a concentric annulus and the $e = r_{ow}$ extreme, which has the center of the inner cylinder on the circumference of the outer, besides being a severe test of the proposed model, represents a circular tube of radius $r_{ow}$.

The hydrodynamic solution of [2] for a concentric annulus of $\gamma = 0.4$ is compared with the ($\varepsilon = 0.001$, $\gamma = 0.4$) solution of the proposed model. While the total pressure defect was found to be 0.67 in [2], a value of 0.710 was obtained in [1] which compares favorably with the 0.714 value obtained in the present analysis. Figure 6 shows the close agreement between $W$ distributions of [2] and that of the present solution.

The $e = r_{ow}$ extreme corresponds to the geometry ($\varepsilon = 1.0$, $\gamma = 0.$). Unfortunately, truncation errors in the present solution increase as $\varepsilon$ approaches 1.0 and $\gamma$ approaches 0. This happens because as the absolute eccentricity increases, more of the interval $0 \leq \eta \leq \pi$ occurs near the narrow part of the annular gap, causing a dense concentration of constant $\eta$ grid lines at this side of the gap and a sparse distribution at the other. The effect of the truncation errors was assessed by solving the fully developed flow with both 24 and 48

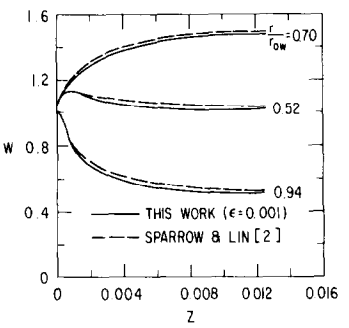


FIG. 6. Comparison of dimensionless axial velocity for $\gamma = 0.4$. This work ($\varepsilon = 0.001$) vs the concentric annulus solution of Sparrow and Lin [2].

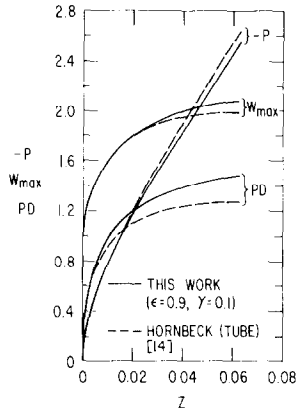


FIG. 7. Comparisons of dimensionless pressure, maximum dimensionless axial velocity, and pressure defect. This work ($\varepsilon = 0.9, \gamma = 0.1$) vs the circular tube solution of Hornbeck [14].

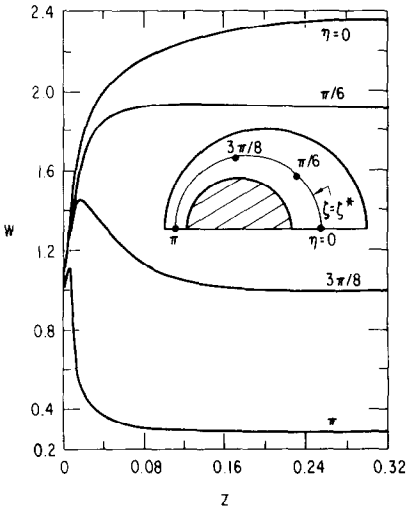


FIG. 8. Dimensionless axial velocity ($\varepsilon = 0.5, \gamma = 0.5$).

equal $\eta$ intervals. From these solutions it was concluded that ($\varepsilon = 0.9, \gamma = 0.1$) is representative of the closest geometry to the desired one for which the truncation errors are acceptable. Hence, in Fig. 7 the present entrance region solution for ($\varepsilon = 0.9, \gamma = 0.1$) is compared with the entrance region solution for a circular tube provided by Hornbeck [14]. Contrary to the assumptions of a similar comparison in [8], the dimensionless variables of the tube and the annulus are defined analogously with the hydraulic diameter of the tube being its diameter and the hydraulic diameter of the annulus being given by equation (25).

A comparison of the fully developed flow solutions of the two geometries provides an indication of how well we can expect the solutions for the entrance region to compare. For this comparison the tube solution is the classical analytical one and the fully developed flow equations of the eccentric annulus were solved with a finite difference grid with 48 equal $\eta$ intervals instead of the 24 used for the entrance region solutions. The annulus as compared to the tube is found to have a $-dP/dZ$ which is 12% smaller and a $W_{max}$ which is 3.8% larger and is displaced $0.056\, r_{ow}$ from the center of the outer cylinder. In spite of these differences, Fig. 7 shows that the present solution compares reasonably well with that of [14]. The close agreement in the figure at $Z = 0$ is a result of the manner in which the dimensionless variables are defined. The assessment of truncation errors in the present solution, as described above, indicates that $W_{max}$ at large $Z$ is about 4% too large. A reduction in the $W_{max}$ of the present solution would make the $W_{max}$ agreement of Fig. 7 even better.

## 5. RESULTS

All eccentric annular geometries are contained within the unit square ($0 \le \varepsilon \le 1, 0 \le \gamma \le 1$). The five geometries ($\varepsilon = 0.9, \gamma = 0.5$), ($\varepsilon = 0.5, \gamma = 0.5$), ($\varepsilon = 0.7, \gamma = 0.3$), ($\varepsilon = 0.9, \gamma = 0.1$), and ($\varepsilon = 0.5, \gamma = 0.1$) were selected for analysis. These were chosen from the quadrant of the unit square with largest $\varepsilon$ and smallest $\gamma$ where the effects of eccentricity are greatest. Typical axial velocity behavior is shown in Fig. 8 which provides $W$ as a function of $Z$. Four values of $\eta$ along the curve $\zeta = \zeta^*$ in the annular cross-section of geometry ($\varepsilon = 0.5, \gamma = 0.5$) are considered. The velocities at $\eta = \pi$ and $\eta = 3/8\,\pi$ each display an initial increase in value near the duct inlet, i.e. $Z = 0$, which is caused by the ejection of flow from the developing boundary layers located along the inner and outer walls. This initial velocity increase is followed by a decrease as fully developed flow values are approached. The velocity distribution at $\eta = \pi/6$ has a barely discernible maximum and at $\eta = 0$ the axial velocity is always increasing and ultimately approaches a maximum asymptotically.

Fully developed flow results provide considerable insight into the effect of geometry on hydrodynamic performance. These results can be obtained by the same methods as those used for a single $Z$ plane of the entrance region except that, since the left-hand side of equation (28) is identically zero, only equations (28) and (31) need be solved. Table 1 provides fully developed flow values of $-dP/dZ$ and $W_{max}$ for the five selected eccentric geometries and the nearly concentric one used in the model verification. In all six cases, including the most eccentric ($\varepsilon = 0.9, \gamma = 0.1$) one, the method of defining $\zeta^*$ was that of the less eccentric geometries. The issue of truncation errors, raised in the previous section, is also addressed by the table. For all five significantly eccentric geometries, the fully developed flow solutions were repeated with 48 equal $\eta$ intervals used in place of 24. These additional results, shown in parentheses, indicate negligible truncations errors for all but the most eccentric geometry, for which the truncation errors are moderate.

All geometries are listed in order of decreasing $\gamma$, and with each group of constant $\gamma$, in order of decreasing $\varepsilon$. The values of $-dP/dZ$ calculated by [18] as tabulated on p. 326 of [19] and shown in brackets in Table 1 are

Table 1. Summary of hydrodynamic results

| Geometry $\varepsilon$ | $\gamma$ | Fully developed flow results $-dP/dZ$ | $W_{max}$ | Total pressure defect | Entrance length* |
|---|---|---|---|---|---|
| 0.9 | 0.5 | 22.84<br>(22.82)†<br>[22.844]‡ | 2.324<br>(2.310) | 2.060 | 0.313 |
| 0.5 | 0.5 | 35.33<br>(35.33)<br>[35.342] | 2.373<br>(2.372) | 2.143 | 0.254 |
| 0.0§ | 0.5 | 47.63 | 1.508 | 0.688¶ | 0.0116¶ |
| $10^{-3}$ | 0.4 | 47.34 | 1.516 | 0.714 | 0.015 |
| 0.0 | 0.4 | 47.36 | 1.513 | | |
| 0.7 | 0.3 | 29.71<br>(29.72)<br>[29.774] | 2.277<br>(2.274) | 1.959 | 0.156 |
| 0.0 | 0.3 | 46.92 | 1.522 | | |
| 0.9 | 0.1 | 28.81<br>(28.17)<br>[28.560] | 2.152<br>(2.076) | 1.571 | 0.106 |
| 0.5 | 0.1 | 36.70<br>(36.71)<br>[36.846] | 2.149<br>(2.148) | 1.535 | 0.0897 |
| 0.0 | 0.1 | 44.69 | 1.567 | 0.784¶ | 0.0175¶ |
| All§ | 0.0 | 32.00 | 2.000 | 1.25¶ | 0.0541¶ |

* The entrance length is taken to be the value of $Z$ at which $W_{max}$ equals 99% of its fully developed flow value.
† All values in parentheses were obtained from the present solution with 48 equal $\eta$ intervals.
‡ All values in brackets were obtained from [18] as tabulated on p. 326 of [19].
§ For concentric annuli all fully developed flow results were obtained from the classical solution.
¶ These data are from the work of [20] as tabulated by [21] and can be found on p. 288 of [19].

in very close agreement with the current solution. Geometries for which either $\varepsilon$ or $\gamma$ is zero are also included for purposes of comparison. The fully developed flow results for these concentric geometries are from the classical closed-form solution. The total pressure defect and entrance length data for these geometries are from the work of [20] as tabulated by [21] and can be found on p. 288 of [19].

The values of $-dP/dZ$ in both Table 1 and Fig. 9 show, as one would expect, that for a fixed $\gamma$, increasing $\varepsilon$ decreases the hydraulic resistance. The values of $W_{max}$ in the table, however, have a trend which is not as predictable. The $\gamma = 0.5$ and the $\gamma = 0.1$ results show that, while a significant increase in $W_{max}$ is observed between $\varepsilon = 0$ and $\varepsilon = 0.5$, the values in parentheses indicate a slight decrease between $\varepsilon = 0.5$ and $\varepsilon = 0.9$. This phenomenon occurs because in the two $\varepsilon = 0.5$ geometries the velocities at the narrowest part of the annular gap are already very low, and further increases in $\varepsilon$ widen the wider part of the gap where flow velocities are large. Since the average velocity is fixed, increasing $\varepsilon$ causes the velocities in the widest part to decrease and thereby lower $W_{max}$.

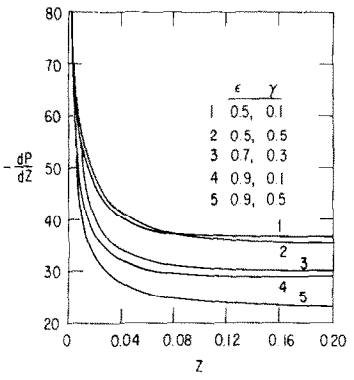


FIG. 9. Dimensionless axial pressure gradients for parametric values of $(\varepsilon, \gamma)$.

In Fig. 10, the two curves for $\gamma = 0.5$ tend to be parallel, as do the two for $\gamma = 0.1$. Had the analysis of the entrance region for the $(\varepsilon = 0.9, \gamma = 0.1)$ geometry been done with a finer mesh, as was possible in the fully developed flow case, the $(\varepsilon = 0.9, \gamma = 0.1)$ curve would probably have remained below the $(\varepsilon = 0.5, \gamma = 0.1)$ curve. This anticipated behavior is consistent with the two $\gamma = 0.5$ curves where the $(\varepsilon = 0.9, \gamma = 0.5)$ curve is below the $(\varepsilon = 0.5, \gamma = 0.5)$ curve. Another observation is that both the figure and the table indicate that the hydrodynamic entrance length increases with increasing $\varepsilon$ or $\gamma$.

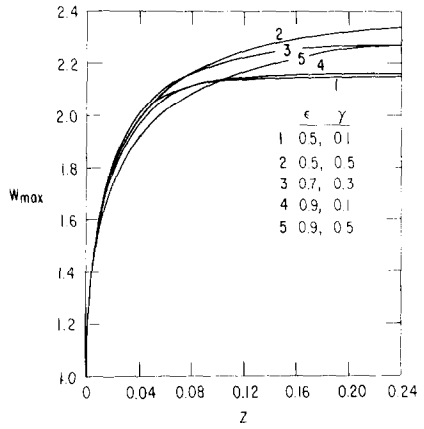


FIG. 10. Maximum dimensionless axial velocity for parametric values of $(\varepsilon, \gamma)$.

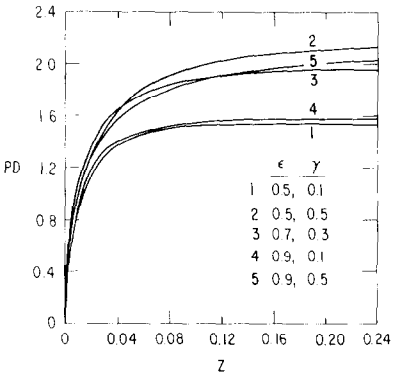


FIG. 11. Pressure defect for parametric values of $(\varepsilon, \gamma)$.

The pressure defect distributions of Fig. 11 parallel the flow developments of Fig. 10. This occurs because the magnitude of the pressure gradient and the wall shear stresses both decrease and the axial momentum increases as the flow develops. This parallel behavior leads one to suspect that, if in Fig. 10 the ($\varepsilon = 0.9, \gamma = 0.1$) curve should be below the ($\varepsilon = 0.5, \gamma = 0.1$) curve, the same should also be true in Fig. 11. One would then conclude that in the table the total pressure defect for the ($\varepsilon = 0.9, \gamma = 0.1$) geometry is less than 1.535, rather than 1.571. In either case, the table indicates that for both $\gamma = 0.1$ and $\gamma = 0.5$ the total pressure defect is almost constant between $\varepsilon = 0.5$ and $\varepsilon = 0.9$. For this range of $\varepsilon$, the table shows a steady decrease in total pressure defect with decreasing $\gamma$, while the concentric geometries display the opposite trend.

Shah and London [19] have compiled hydrodynamic data in a form which is practical for use by designers of compact heat exchangers. As indicated by the reference, data generated by the present analysis was transmitted by private communication. From this data, which included $P$ tabulated as a function of $Z$, they provide friction factor tabulated as a function of $Z$ for the five significantly eccentric geometries of the present analysis. Since the current nomenclature does not agree with that of [19], the Appendix compares essential variables of the two nomenclatures.

## 6. CONCLUSIONS

The solution of the hydrodynamic entrance region was obtained from analysis of the proposed hydrodynamic model. This model was developed from an order of magnitude anslysis of the Navier–Stokes equations and a transverse flow description which was based on physical arguments. Other transverse flow descriptions were tested as part of the verification of the model and were shown to produce similar results. The solution of the proposed hydrodynamic model for the geometry ($\varepsilon = 0.001, \gamma = 0.4$) compared rather well with the solution of [2] for concentric annuli, and the results for the rather eccentric geometry ($\varepsilon = 0.9, \gamma = 0.1$) compared reasonably well with the solution of [14] for the circular tube.

Some of the salient aspects of the numerical methods used to solve the equations of the entrance region model are: (1) the use of both variable axial step sizes and variable $\zeta$ intervals in the finite difference grid, (2) the use of Allen's method in the finite difference representation of the axial momentum equation, and (3) the use of a modified version of the S.O.R. method in which Aitken's $\Delta^2$ method is used to accelerate the convergence of the iterates of $dP/dZ$.

The results of the current analysis quantify some of the perhaps foreseeable effects of eccentricity on annular geometries such as longer hydrodynamic entrance lengths and lower hydraulic resistance with increasing $\varepsilon$. The behavior of the total pressure defect, however, is less predictable. For concentric annuli, it decreases with increasing $\gamma$ while some of the eccentric geometries display the opposite trend. Moreover, for some values of $\gamma$, the total pressure defect increases dramatically between $\varepsilon = 0$ and $\varepsilon = 0.5$, but remains relatively constant between $\varepsilon = 0.5$ and $\varepsilon = 0.9$.

In conclusion, the numerical marching techniques described by [12] and used by [11] to analyze the hydrodynamic entrance region of a square duct, have been extended to the eccentric annulus. In addition to providing data, the present solution demonstrates modeling and numerical techniques which are applicable to ducts of other configurations.

## REFERENCES

1. T. S. Lundgren, E. M. Sparrow, and J. B. Starr, Pressure drop due to the entrance region in ducts of arbitrary cross section, *J. basic Engng, Trans. ASME* **86**, 620–626 (1964).
2. E. M. Sparrow and S. H. Lin, The developing laminar flow and pressure drop in the entrance region of annular ducts, *J. basic Engng, Trans. ASME* **86**, 827–834 (1964).
3. Katsuhisa Murakawa, Heat transfer in entry length of double pipes, *Int. J. Heat Mass Transfer* **2**, 240–251 (1961).
4. H. S. Heaton, W. C. Reynolds and W. M. Kays, Heat transfer in annular passages. Simultaneous development of velocity and temperature fields in laminar flow, *Int. J. Heat Mass Transfer* **7**, 764–781 (1964).

5. R. W. Shumway and D. M. McEligot, Heated laminar gas flow in annuli with temperature-dependent transport properties, *Nucl. Sci. Engng* **46**, 394–407 (1971).
6. P. J. Redberger and M. E. Charles, Axial laminar flow in a circular pipe containing a fixed eccentric core, *Can. J. chem. Engng* **40**, 148–151 (1962).
7. W. T. Snyder and G. A. Goldstein, An analysis of fully developed laminar flow in an eccentric annulus, *AIChE Jl* **11**, 462–467 (1965).
8. E. E. Feldman, The numerical solution of the combined thermal and hydrodynamic entrance region of an eccentric annular duct. Ph.D. thesis, Carnegie-Mellon University, Pittsburgh, PA (1974).
9. J. T. Wilson, Analysis of fluid flow in the entrance region of a duct with an eccentric annular cross-section. Ph.D. thesis, University of Houston, Houston, TX (1974).
10. W. F. Hughes and E. W. Gaylord, *Basic Equations of Engineering Science*, Schaum, New York (1964).
11. G. A. Carlson and R. W. Hornbeck, A numerical solution for laminar entrance flow in a square duct, *J. appl. Mech. Trans. ASME* **40**, 25–30 (1973).
12. R. W. Hornbeck, Numerical marching techniques for fluid flows with heat transfer, NASA SP-297, Washington, D.C. (1973).
13. J. R. Bodoia, The finite difference analysis of confined viscous flows. Ph.D. thesis, Carnegie Institute of Technology, Pittsburgh, PA (1959).
14. R. W. Hornbeck, Laminar flow in the entrance region of a pipe, *Appl. Sci. Res.* **13(A)**, 224–232 (1964).
15. D. N. de G. Allen and R. V. Southwell, Relaxation methods applied to determine the motion, in two dimensions, of a viscous fluid past a fixed cylinder, *Q. J. Mech. appl. Math.* **8**, 129–145 (1955).
16. Peter Henrici, *Elements of Numerical Analysis*, pp. 70–74. John Wiley, New York (1964).
17. J. R. Westlake, *A Handbook of Numerical Matrix Inversion and Solution of Linear Equations*, pp. 83–84. John Wiley, New York (1968).
18. W. Tiedt, Berechnung des Laminaren und Turbulenten Reibungswiderstandes Konzentrischer und Exzentrisher Ringspalte. Part I., *Chem. Ztg., Chem. Appar.* **90**, 813–821 (1966); Part II., *Chem. Ztg., Chem. Appar.* **91**, 17–25 (1967); also as Tech. Ber. 4 Inst. Hydraul. Hydrol., Technische Hochschule, Darmstadt (1968); English translation-Transl. Bur. No. 0151, p. 248, Transp. Dev. Agency Libr., Montreal (1971).
19. R. K. Shah and A. L. London, *Laminar Flow Forced Convection in Ducts*. Academic Press, New York (1978).
20. V. L. Shah and K. Farnia, Flow in the entrance of annular tubes, *Computers and Fluids* **2**, 285–294 (1974).
21. J. Liu, Flow of Binghan fluids in the entrance region of an annular tube. M.S. thesis, University of Wisconsin, Milwaukee, WI (1974).

## APPENDIX

Since Shah and London [19] on pp. 333–336 provide data generated by the current analysis, a nomenclature comparison is provided in Table A1.

Table A1. Nomenclature comparison

| Shah and London [19] | Current analysis |
|---|---|
| $e^*$ | $\varepsilon$ |
| $f_{app}Re$ | $-P/(2Z)$ |
| $K(\infty)$ | $PD$ for fully developed flow |
| $L_{hy}$ | value of $Z$ at which the maximum $W$ has reached 99% of its fully developed flow value |
| $r^*$ | $\gamma$ |
| $u_{max}/u_m$ | $W_{max}$ for fully developed flow |
| $x^+$ | $Z$ |

## UNE SOLUTION NUMERIQUE DE L'ECOULEMENT LAMINAIRE EN DEVELOPPEMENT DANS LES CONDUITES ANNULAIRES EXCENTRIQUES

**Résumé**—On analyse l'écoulement laminaire incompressible dans des conduites droites dont la section est annulaire excentrique. Des méthodes numériques sont utilisées pour résoudre un modèle hydrodynamique approché qui est développé à partir des équations de Navier–Stokes en représentation par coordonnées bipolaires. Des solutions obtenues se comparent favorablement à celles des modèles alternés et à des solutions publiées pour l'anneau concentrique et le tube circulaire. Des résultats sont présentés pour cinq géométries différentes.

## EINE NUMERISCHE LÖSUNG FÜR DIE LAMINARE ANLAUFSTRÖMUNG IN EXZENTRISCHEN RINGKANÄLEN

**Zusammenfassung**—Es wird die laminare inkompressible Strömung in geraden Kanälen mit exzentrischem ringförmigem Querschnitt untersucht. Numerische Methoden werden angewandt, um ein hydrodynamisches Näherungsmodell zu lösen, das aus der Bipolarkoordinatendarstellung der Navier–Stokes-Gleichungen entwickelt wurde. Die Lösungen des vorgeschlagenen Modells lassen sich gut mit den Lösungen zweier alternativer Modelle und mit veröffentlichten Lösungen für den konzentrischen Ringraum und das Kreisrohr vergleichen. Für fünf verschiedene Geometrien werden Ergebnisse angegeben.

## ЧИСЛЕННЫЙ РАСЧЕТ ЛАМИНАРНОГО НЕУСТАНОВИВШЕГОСЯ ТЕЧЕНИЯ В ЭКСЦЕНТРИЧЕСКИХ КОЛЬЦЕВЫХ КАНАЛАХ

**Аннотация** — Анализируется ламинарное течение несжимаемой жидкости в прямых каналах эксцентрического кольцевого сечения. Для решения приближенной гидродинамической модели, основанной на выраженных в биполярных координатах уравнениях Навье–Стокса, используются численные методы. Результаты решения хорошо согласуются с данными, полученными с помощью двух других моделей и с опубликованными решениями для концентрического кольцевого канала и круглой трубы. Результаты представлены для пяти различных геометрий.